

AMSU-B Observations of Mixed-Phase Clouds over Land

M. N. DEETER AND J. VIVEKANANDAN

Research Applications Program, National Center for Atmospheric Research, Boulder, Colorado*

(Manuscript received 29 July 2003, in final form 13 July 2004)

ABSTRACT

Measurements from passive microwave satellite instruments such as the Advanced Microwave Sounding Unit B (AMSU-B) are sensitive to both liquid and ice cloud particles. Radiative transfer modeling is exploited to simulate the response of the AMSU-B instrument to mixed-phase clouds over land. The plane-parallel radiative transfer model employed for the study accounts for scattering and absorption from cloud ice as well as absorption and emission from trace gases and cloud liquid. The radiative effects of mixed-phase clouds on AMSU-B window channels (i.e., 89 and 150 GHz) and water vapor line channels (i.e., 183 ± 1 , 3, and 7 GHz) are studied. Sensitivities to noncloud parameters, including surface temperature, surface emissivity, and atmospheric temperature and water vapor profiles, are also quantified. Modeling results indicate that both cloud phases generally have significant radiative effects and that the 150- and 183 ± 7 -GHz channels are typically the most sensitive channels to integrated cloud properties (i.e., liquid water path and ice water path). However, results also indicate that AMSU-B measurements alone are probably insufficient for retrieving all mixed-phase cloud properties of interest. These results are supported by comparisons of AMSU-B observations of a mixed-phase cloud over the Atmospheric Radiation Measurement (ARM) Program's Southern Great Plains (SGP) site with corresponding calculated clear-sky values.

1. Introduction

Although mixed-phase clouds are relatively common (Riley 1998), remote sensing techniques specifically tailored to retrieve their physical properties [e.g., ice water content (IWC) and liquid water content (LWC)] are much less common than techniques developed for single-phase clouds. One remote sensing technique for studying mixed-phase clouds exploits multiple ground-based instruments, which are able to separately monitor the individual phases (e.g., Vivekanandan et al. 1997). Specifically, ground-based passive microwave measurements of the liquid water path (LWP; exploiting measurements at 20 and 31 GHz) are typically assumed to be insensitive to nonprecipitating ice particles (Westwater 1993), whereas radar reflectivity is heavily dominated by properties of the ice water path (IWP; Vivekanandan et al. 1997). In contrast, the radiative effects of both phases should be considered in studies of nonprecipitating mixed-phase clouds based on passive measurements in the visible and infrared spectral re-

gions (Baum et al. 2000), and for microwaves with frequencies greater than about 90 GHz (Deeter and Evans 2000; Greenwald et al. 1999). Thus, when remote sensing techniques developed for single-phase clouds are applied to mixed-phase clouds, the presence of the neglected phase can generally pose a serious source of retrieval error. Here, we report forward-modeling simulations, which demonstrate that both phases may produce significant radiative effects at operational millimeter-wave frequencies between 89 and 183 GHz. These simulations have direct relevance to the application of single-phase millimeter-wave retrieval algorithms on mixed-phase clouds. In addition, we present a case study to demonstrate empirically that mixed-phase clouds over land produce measurable radiative effects at operational millimeter-wave frequencies.

Satellite remote sensing offers features (global coverage, regular sampling, etc.) for observational atmospheric studies that are not readily achieved using either in situ sampling or ground-based remote sensing techniques. However, interpretation of remote sensing observations of clouds requires a detailed understanding of both cloud properties and radiative transfer. Passive satellite sensors have been used to classify and quantify cloud properties for decades. These systems either operate in the shortwave (visible and near-infrared), thermal infrared, or microwave spectral regions. Of the three, microwave systems are the most

* The National Center for Atmospheric Research is sponsored by the National Science Foundation.

Corresponding author address: M. N. Deeter, National Center for Atmospheric Research, P.O. Box 3000, Boulder, CO 80307.
E-mail: mnd@ucar.edu

capable of probing thick clouds. Millimeter-wave sensors (microwave systems operating at frequencies between about 30 and 300 GHz) respond to radiation at wavelengths considerably larger than typical cloud particles, whereas shortwave and thermal infrared sensors respond to wavelengths much smaller than typical cloud particles. Mie theory predicts that the extinction efficiency Q of typical cloud particles exposed to shortwave and thermal infrared radiation should be on the order of unity, but should be much smaller than unity for cloud particles exposed to microwave radiation (Goody and Yung 1995). Thus, for the same cloud, optical depths are generally much larger for shortwave and thermal infrared sensors than for microwave systems. In practical terms, this distinction implies that shortwave and thermal infrared techniques are usually most useful for deducing cloud-top properties (e.g., cloud-top temperature), whereas microwave techniques often provide a more direct measure of vertically integrated cloud properties (e.g., liquid water path). In this paper, we attempt to quantify the sensitivity of satellite-based millimeter-wave sensors to mixed-phase cloud properties, including cloud vertical structure, liquid water path, ice water path, and ice particle size. Results of this study should be useful for guiding the development of future cloud classification and retrieval algorithms for studying mixed-phase clouds using satellite-based millimeter-wave radiometers. Results presented here also indicate that the application to mixed-phase clouds, of millimeter-wave-based retrieval algorithms developed specifically for single-phase clouds, is generally not appropriate.

In the next section, we review current satellite-based millimeter-wave sensors that could potentially be exploited for characterizing mixed-phase clouds. In section 3, we describe the radiative transfer models and cloud models used to simulate millimeter-wave measurements of mixed-phase clouds. Simulation results are then presented that show the sensitivity of the observations both to clear-sky parameters (e.g., surface temperature and emissivity) and to mixed-phase cloud parameters. Last, simultaneous Advanced Microwave Sounding Unit B (AMSU-B) observations and ground-based remote sensing observations of a system of non-precipitating clouds at the Atmospheric Radiation Measurements (ARM) Program's Southern Great Plains (SGP) site in March 2002 are used to demonstrate the effects of a particular mixed-phase cloud on the AMSU-B channels, and to test some qualitative predictions from modeling.

2. Cloud studies using millimeter-wave radiometry

Beginning with the Special Sensor Microwave Temperature Profiler 2 (SSM/T-2) satellite instrument on the Defense Meteorological Satellite Program (DMSP) satellite platforms, a standard configuration of five millimeter-wave channels has emerged. Similar satellite-

based instruments include AMSU-B on the current National Oceanic and Atmospheric Administration (NOAA)-K/-L/-M satellites and the Humidity Sensor for Brazil (HSB) (Jet Propulsion Laboratory 2000) on the Earth Observing System (EOS) *Aqua* platform (online at <http://aqua.nasa.gov>). With the exception of HSB (which lacks only the 89-GHz channel), all of these instruments are equipped with two "window channels" near 89 and 150 GHz, and three "water vapor line channels" centered on the water vapor absorption line at 183.3 GHz. The primary intended function of these instruments is to enable retrievals of water vapor profiles even in cloudy conditions (which is not feasible using infrared sensors, such as HIRS).

a. Single-phase clouds versus mixed-phase clouds

Both observational and modeling studies have previously considered the sensitivity of these instruments' observations to cloud liquid water, cloud ice, and various forms of precipitation (Burns et al. 1997; Isaacs and Deblonde 1987; Muller et al. 1994). These studies demonstrated clearly that, although millimeter-wave radiation penetrates both liquid and ice clouds more readily than do visible or infrared radiation, the radiative sensitivity of millimeter waves to clouds is not generally negligible. None of these studies, however, specifically considered millimeter-wave observations of mixed-phase clouds. Because radiation at millimeter wavelengths is sensitive to both liquid and ice particles, interpretation of observations of mixed-phase clouds is substantially more complicated than for single-phase clouds. For this reason, perhaps, retrieval algorithms for extracting cloud properties from millimeter-wave sensor data have so far assumed single-phase clouds consisting of either pure liquid (Rosenkranz 2001) or pure ice (Zhao and Weng 2002). Neither of these algorithms were developed to treat mixed-phase clouds, and, therefore, should not strictly be applied in cases where mixed-phase conditions might occur.

On the other hand, the fact that the interaction of millimeter-wave radiation with liquid and ice particles involves different physical mechanisms suggests the possibility of developing retrieval algorithms that independently retrieve both liquid and ice cloud characteristics (e.g., liquid water path and ice water path). Typically, liquid cloud particles respond to millimeter waves primarily through absorption and emission, whereas scattering processes dominate in the radiative response for ice particles. At the very least, millimeter-wave observations may provide information on mixed-phase clouds, which complements information from more standard instrumentation (e.g., radar and lower-frequency microwave measurements).

b. Window channels versus water vapor line channels

Satellite- and aircraft-based millimeter-wave retrieval algorithms for retrieving cloud properties have

so far primarily exploited window channels (e.g., 89, 150, and 220 GHz) because of the interfering effect of water vapor on the water vapor line channels (Deeter and Evans 2000; Liu and Curry 2000; Zhao and Weng 2002). Under clear-sky conditions, observed brightness temperatures for the water vapor line channels primarily depend on the atmospheric temperature and water vapor vertical profiles. Thus, interpretation of observations of cloudy scenes using millimeter-wave window channels does not require consideration of the atmospheric temperature or humidity to the same degree that it would for the water vapor line channels. On the other hand, because of the much higher atmospheric transmittance, the use of millimeter-wave window channels requires greater consideration of the variable effects of surface temperature and emissivity. When these surface parameters are known and relatively constant (e.g., over the tropical oceans), millimeter-wave window channels have a more direct response to clouds than the water vapor line channels. (Microwave cloud retrievals over oceanic scenes also benefit from the low emissivity of the ocean surface, because this results in greater thermal contrast between the atmosphere and underlying surface.) Over land, however, surface temperature and emissivity are both highly variable, and must be explicitly considered when studying window channel observations. For example, several authors (Greenwald et al. 1997; Jones and Vonder Haar 1990) have demonstrated the importance of surface emissivity variability to retrievals of liquid water path over land using the SSM/I 85-GHz channel.

Thus, over land, the water vapor line channels may prove to be more valuable than (or at least complementary to) the window channels because of their decreased sensitivity to surface parameters. Moreover, as shown below (in section 3b), the higher frequency of the water vapor line channels should make them more sensitive to both liquid and ice cloud particles. Last, because of the much narrower weighting functions of the water vapor line channels (relative to the window channels), they offer greater potential for resolving cloud vertical structure. A similar concept for studying cloud vertical structure was previously considered for an instrument with channels near the 118-GHz oxygen absorption line (Gasiewski 1993).

3. Modeling strategies

In this section, we describe the radiative transfer model used to explore the sensitivity of the AMSU-B channels to mixed-phase cloud properties. Precipitating clouds are not treated here. Specifically, we consider wintertime midlevel, mixed-phase clouds over land because of their association with aircraft icing conditions (Cober et al. 2001; Politovich 1989; Riley 1998). The objective of this research is to quantify the sensitivity of the AMSU-B channels to mixed-phase cloud properties, including cloud vertical structure, liquid water

path, ice water path, and ice particle size. Results of this study should be useful for guiding the development of future cloud classification and retrieval algorithms for studying mixed-phase clouds using satellite-based millimeter-wave radiometers. More specifically, the results presented here should be considered before applying retrieval algorithms developed for single-phase clouds to mixed-phase clouds.

For radiance I and optical depth τ , the nonpolarized radiative transfer equation (RTE) for a thermally emitting atmosphere may be written

$$\mu \frac{dI(\tau, \mu)}{d\tau} = I(\tau, \mu) - J(\tau, \mu) = I(\tau, \mu) - \left[\frac{\omega}{2} \int_{-1}^1 I(\tau, \mu') P(\mu, \mu') d\mu' + B(\tau)(1 - \omega) \right], \quad (1)$$

where μ and μ' are the cosines of the observed and incident zenith angles, $J(\tau, \mu)$ is the source function, ω is the single scattering albedo, $P(\mu, \mu')$ is the scattering phase function, and $B(\tau)$ is the Planck function (Goody and Yung 1995). For the case of millimeter-wave radiation interacting with liquid and ice cloud particles, both thermal emission and scattering sources are potentially important and have, therefore, been retained in the RTE. For a polydispersed distribution of spheres of concentration (number per unit volume per unit incremental diameter) $N(D)$, the optical depth τ is related to the vertical coordinate z through the relation

$$\frac{d\tau}{dz} = \beta = \int_0^\infty \pi \left(\frac{D}{2} \right)^2 Q(D) N(D) dD, \quad (2)$$

where β is the volume extinction coefficient and $Q(D)$ is the extinction efficiency factor. Here, $Q(D)$ can further be written as the sum of absorptive and scattering components, that is,

$$Q(D) = Q_a(D) + Q_s(D). \quad (3)$$

Generally, Q_a and Q_s depend on particle size and shape, the radiation wavelength, and the complex refractive index m .

a. Microphysical properties

For the mixed-phase cloud radiative transfer calculations reported in this work, liquid cloud particles are assumed to be spherical. We also assume a solid sphere model for ice particles, despite the highly variable bulk density and habits of ice particles actually observed in cirrus and mixed-phase clouds. Evans et al. (Evans and Stephens 1995; Evans and Vivekanandan 1990; Evans et al. 1998) demonstrated that the radiometric sensitivity at millimeter-wave frequencies for cirrus particles varies substantially (up to a factor of 2 or 3) with particle shape. However, the sensitivity (e.g., extinction) for solid ice spheres was often found to be intermediate with respect to the sensitivity for more realistic habits

(columns, rosettes, etc.). Thus, for microwave radiative transfer, the solid ice sphere is a reasonable nominal ice particle-shaped model. Effects due to the nonsphericity and varying bulk density of actual ice particles will be explored in future research.

Cloud particle size distributions must be specified in order to calculate the basic cloud radiative properties, that is, the single scattering properties (extinction, single scattering albedo, and scattering phase function). For both liquid and ice water particles, we employ the standard gamma distribution to model the particle size variability. By convention, the gamma distribution is written.

$$N(D) = aD^\alpha \exp\left[-\frac{(\alpha + 3.67)D}{D_0}\right], \quad (4)$$

where N is the concentration (number of particles per unit volume per unit incremental diameter) of spherical particles of diameter D , a is a scaling factor related to the liquid or ice water content (i.e., liquid or ice mass per unit volume), α defines the width of the distribution, and D_0 is the median diameter of the distribution (Evans et al. 1998). The three parameters in the distribution independently control the integrated mass density (liquid or ice water content), characteristic particle size, and distribution width.

Ice particle size in mixed-phase clouds often exhibits much greater variability than liquid particle size. Nevertheless, we consider the dependence of single scattering properties on particle size for both phases. For liquid cloud particles, we consider median diameters between 10 and 100 μm . In nonprecipitating clouds, observed liquid cloud droplets are typically less than 40 μm in diameter (Liou 1992). For ice particles, we consider median diameters between 10 and 500 μm . Particles with maximum dimensions of hundreds of microns have been observed in the lower regions of nonprecipitating mixed-phase clouds (e.g., Fleishauer et al. 2002).

b. Single scattering properties

Scattering properties are often expressed in terms of the size parameter x defined as

$$x \equiv \pi D/\lambda, \quad (5)$$

where λ is the radiation wavelength. The Rayleigh scattering regime is strictly valid when $x \ll 1$ for all particles in a given distribution. Although this limit is not perfectly obeyed for all of the particle sizes and radiative wavelengths considered in this work, Rayleigh scattering may be considered a good first-order model for understanding the roles of millimeter-wave absorption and scattering in mixed-phase clouds. (Actual modeling results presented in section 4 are based on Mie scattering theory rather than Rayleigh scattering theory.) For spherical particles of the complex refractive index m ,

the absorption and scattering efficiency factors in the Rayleigh limit are

$$Q_a(x) = 4x \operatorname{Im}\left(\frac{m^2 - 1}{m^2 + 2}\right) \quad (6)$$

and

$$Q_s(x) = \frac{8x^4}{3} \left|\frac{m^2 - 1}{m^2 + 2}\right|^2. \quad (7)$$

By resolving τ into its absorptive and scattering components τ_a and τ_s , we find from Eqs. (2), (6), and (7) that

$$\frac{d\tau_a}{dz} = \frac{8\pi}{\lambda} \operatorname{Im}\left(\frac{m^2 - 1}{m^2 + 2}\right) \int_0^\infty \pi \left(\frac{D}{2}\right)^3 N(D) dD \quad (8)$$

and

$$\frac{d\tau_s}{dz} = \frac{8}{3} \left[\frac{(2\pi)}{\lambda}\right]^4 \left|\frac{m^2 - 1}{m^2 + 2}\right|^2 \int_0^\infty \pi \left(\frac{D}{2}\right)^6 N(D) dD. \quad (9)$$

These equations indicate that τ_a is proportional to the third moment of $N(D)$, whereas τ_s is proportional to the sixth moment. The third moment of $N(D)$ is proportional to the total volume occupied by the cloud particles of a given distribution and, therefore, represents liquid or ice mass (assuming that particle mass density is fixed). In contrast, the scattering optical depth τ_s is primarily determined by the largest particles in the particle size distribution (through the sixth moment), and increases rapidly with increasing particle size.

The use of the solid-sphere model for both liquid and ice cloud particles allows the use of Mie theory for calculating single scattering properties, including extinction, single scattering albedo (defined as the ratio of the scattering extinction coefficient and the total extinction coefficient), and asymmetry parameter (i.e., the first moment of the scattering phase function) (Liou 1992). For homogeneous spherical scatterers, Mie theory is exact (and, therefore, applicable to size parameters well outside of the Rayleigh regime). Calculated values of extinction, the single scattering albedo, and the asymmetry parameter are plotted against the median diameter D_0 for gamma distributions of liquid water and ice spheres in Figs. 1 and 2. In all single scattering calculations, the median particle size was varied, whereas the liquid water content (or ice water content for solid spheres) was kept fixed at 1 g m^{-3} . The phase- and frequency-dependent complex refractive index of water is taken from Ray (1972). In both figures, the curves labeled “183.3 GHz” represent the single scattering properties for all three AMSU-B water vapor line channels. Because all three of these channels are centered on the same frequency, and because of the relatively weak variability of the single scattering properties over the frequency range from 175 to 191 GHz

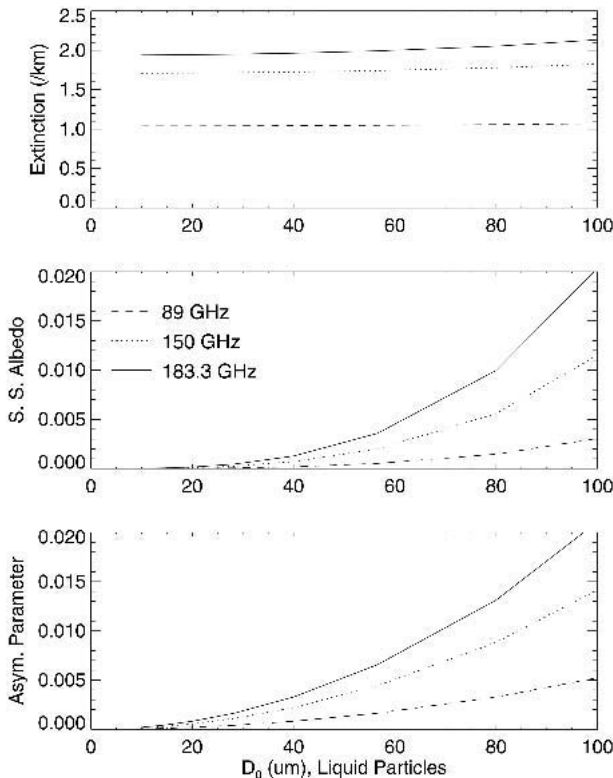


FIG. 1. Single scattering properties—(top) extinction, (middle) single scattering albedo, and (bottom) asymmetry parameter—of liquid water spheres for three AMSU-B microwave bands as a function of median diameter. Extinction is calculated for fixed liquid water content of 1 g m^{-3} .

(the bounding frequency limits for the three channels), the single scattering properties may be assumed to be the same for all three channels.

As indicated by Fig. 1, the single scattering albedo for liquid spheres is much less than one throughout the range of expected cloud particle size. Scattering from liquid cloud particles may, therefore, be assumed to be insignificant for the AMSU-B channels. Previous work indicates that scattering in liquid clouds may be justifiably neglected at AMSU-B frequencies when the mode radius is less than about $20 \mu\text{m}$ (Muller et al. 1994). As described previously, the prevalence of absorption over scattering in the Rayleigh limit (i.e., for particles much smaller than the radiation wavelength) theoretically produces extinction that is proportional to the third moment of the particle size distribution, which represents liquid water content (liquid mass per unit volume). Because liquid water content was kept fixed during single scattering calculations, the extinction should exhibit negligible dependence on the liquid sphere median particle size. This prediction is confirmed in the top panel of Fig. 1, up to the typical maximum diameter of liquid cloud particles ($\sim 40 \mu\text{m}$). The monotonic increase of extinction with millimeter-wave frequency evident in the figure is also consistent with the absorp-

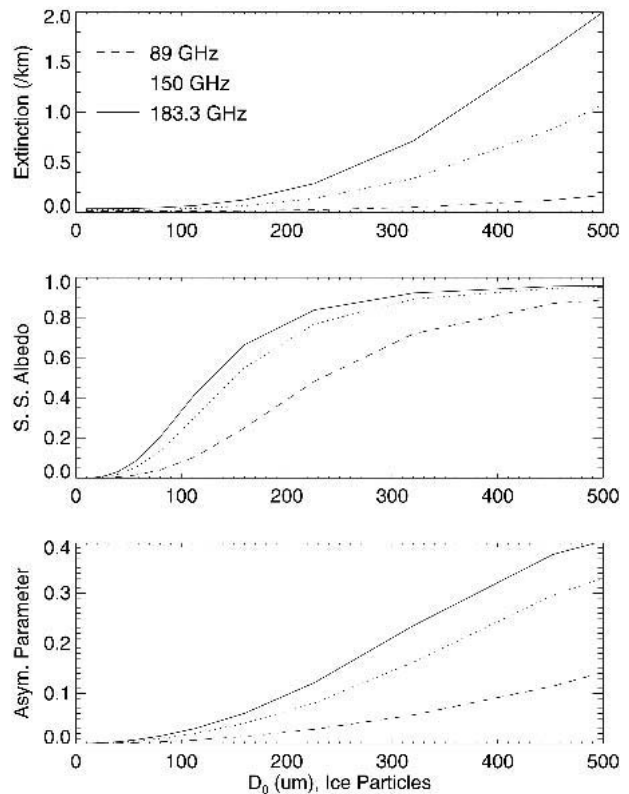


FIG. 2. As in Fig. 1, single scattering properties of ice spheres for the three AMSU-B microwave bands as a function of median diameter. Extinction is calculated for fixed ice water content of 1 g m^{-3} .

tive Rayleigh limit (size parameter x increases linearly with frequency).

In the millimeter-wave spectral range, $\text{Im}(m)$ (i.e., the absorptive component) for liquid water exceeds $\text{Im}(m)$ for ice by more than two orders of magnitude (Ray 1972). Therefore, for particles of similar size, the single scattering albedo for ice particles should be much larger than for liquid water particles. This predicted behavior is confirmed by comparing the middle panels of Figs. 1 and 2. For ice spheres, the prevalence of scattering introduces a strong particle-size dependence to the extinction, unlike the case for liquid water spheres. In the Rayleigh limit, scattering-dominated extinction increases as the sixth moment of the particle size distribution. The relatively weak extinction for ice particles smaller than about $100\text{--}200 \mu\text{m}$ indicates that such particles are effectively insignificant at millimeter-wave frequencies. For example, the extinction produced by liquid phase particles (with equivalent liquid water content) is more than an order of magnitude greater than for ice particles with D_0 values less than $200 \mu\text{m}$.

c. Radiative transfer modeling

For mixed-phase cloud radiative transfer simulations, we employed a modified two-stream scattering model.

The plane-parallel radiative transfer model RTSPEC (available online at <http://nit.colorado.edu>) accounts for absorption and scattering processes using a hybrid technique that integrates the single scattering solution with the Eddington solution (Deeter and Evans 1998). While nearly as computationally efficient as the Eddington solution, the hybrid solution retains more information regarding the scattering phase function. (The Eddington solution relies on just a single moment of the scattering phase function.) This is particularly important under conditions of weak scattering (i.e., small to moderate scattering optical depths), which is often the case in microwave atmospheric remote sensing.

Before executing RTSPEC, the user must compute layer absorption optical depths over the spectral range of interest for the atmosphere being modeled. For that purpose, we employed the MONORTM radiative transfer code from Atmospheric and Environmental Research, Inc. (available online at <http://rtweb.aer.com>). Layer optical depths were calculated on a grid with 1-km vertical resolution and at a spectral resolution of 0.002 cm^{-1} (approximately 60 MHz). Absorption effects due to both gases and liquid water particles (representing the liquid component of mixed-phase clouds) are explicitly included in the layer optical depth calculations. Based on the conclusion above that scattering is insignificant for liquid cloud particles at AMSU-B frequencies, we neglect it completely. This assumption is equivalent to the approximation that the single scattering albedo for liquid-phase cloud particles is exactly zero. In this limit, the radiative properties of the liquid component of mixed-phase clouds depend on the liquid water content (liquid mass per unit volume), but not on liquid particle size. For the same reason, the assumed size distribution plays no role in the radiative transfer calculations.

d. Cloud models

The most simple mixed-phase cloud model is one in which both liquid and ice particles are assumed to be homogeneously distributed within a single layer. More complex two- and three-layer models have also been considered in which the top layer is populated exclusively by ice particles and the bottom layer by liquid droplets (Zhang and Vivekanandan 1999). Previous microwave modeling results for ground-based remote sensing studies indicate that substantial brightness temperature differences (on the order of 10 K) may result from the choice of the mixed-phase cloud model (Zhang and Vivekanandan 1999). We considered three plane-parallel models to represent the geometrical (macrophysical) characteristics of mixed-phase clouds. The uniform mixing (UM) model is a single-layer model characterized by cloud-base and cloud-top heights of 3 and 6 km, respectively. Within those boundaries, both LWC and IWC are assumed to be homogeneous. The glaciated cloud-top (GT) model is characterized by a homogeneous liquid cloud layer be-

tween 3 and 5 km, and a homogeneous ice cloud layer between 5 and 6 km. Finally, the glaciated cloud-base (GB) model is characterized by a liquid cloud layer between 4 and 6 km, and an ice cloud layer between 3 and 4 km. All three cloud models exhibit the same cloud-top and cloud-base heights, although with substantially different distributions of ice and liquid mass.

Inclusion of the GB model is consistent with the observation of large ice particles (and a peak in IWC) near the bottoms of some mixed-phase clouds (Fleishauer et al. 2002). Because the extinction associated with ice particles increases rapidly with particle size, the vertical distribution of the largest particles will have a much stronger effect on radiative transfer modeling results than will the distribution of smaller ice particles. Although the actual macrophysical characteristics of mixed-phase clouds are extremely variable, the three models considered here should provide a constructive basis to simulate the effects of ice and liquid vertical distribution on AMSU-B observations.

For each cloud model, the IWP (or vertically integrated IWC) within the ice cloud layer and the LWP within the liquid cloud layer were independently varied. Radiative transfer calculations were carried out for each cloud model over a grid of IWP and LWP values, and for two ice particle D_0 values: 200 and 400 μm . These two D_0 values were selected to demonstrate the significant role played by ice particle size in determining radiative properties. (For ice particle distributions, a value of 7 was assumed for α . This choice represents a relatively narrow distribution in order to accentuate the role played by particle size. Sensitivity of the radiative transfer model results to α will be addressed in future studies.)

e. Other modeling parameters

For the “baseline” atmospheric state (i.e., the nominal temperature and water vapor vertical profiles), we chose the McClatchey midlatitude winter profile (Ellingson et al. 1991). However, for consistency with the cloud models described above, the water vapor vertical profile was modified between 3 and 6 km by setting the relative humidity (with respect to ice) within that layer to 100%. Monochromatic clear-sky weighting functions (derivatives of transmittance with respect to height) representing each of the AMSU-B channels for the revised McClatchey midlatitude winter profile are shown in Fig. 3. (Weighting functions were calculated on a 1-km grid, and then smoothed using cubic spline interpolation.) The McClatchey midlatitude winter profile was selected for this study as a reasonable model for representing wintertime continental interior conditions. Surface temperature was taken as the temperature in the atmospheric profile closest to the surface (272.2 K). Surface emissivity was set to 0.9 for all AMSU-B channels because, over land, typical surface emissivity values at millimeter-wave frequencies range from about 0.8 to 1.0 (Felde and Pickle 1995).

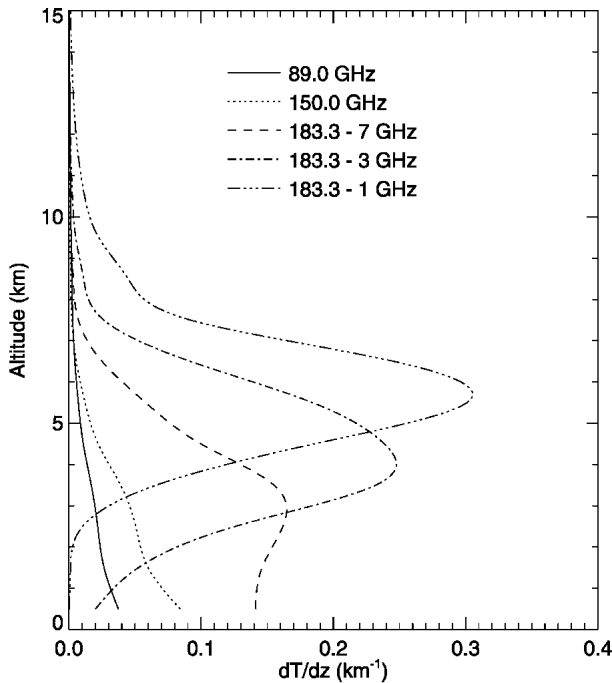


FIG. 3. Clear-sky weighting functions (derivatives of transmittance with respect to altitude) for the AMSU-B channels and the modified McClatchey midlatitude winter profile. Weighting functions were calculated on a 1-km grid and then smoothed by cubic spline interpolation. Results were calculated from monochromatic layer optical depths calculated by MONORTM for the nadir view at 89.0, 150.0, 176.3, 180.3, and 182.3 GHz. (Actual radiative transfer simulations performed with RTSPEC include spectral integration over the instrumental bandpasses. The monochromatic weighting functions shown here describe the radiance sensitivity at the spectral center of each channel.)

4. Simulation results

Prior to simulating the effects of varying cloud parameters on the AMSU-B brightness temperatures, clear-sky simulations were performed to quantify the first-order sensitivity of the brightness temperatures to relative humidity, atmospheric and surface temperature, and surface emissivity. Because in real applications these geophysical parameters will generally be characterized by some uncertainty, each represents a potential source of error in any satellite-based mixed-

phase cloud retrieval algorithm. Four test cases were conducted in which perturbations were separately applied to 1) the relative humidity (RH) profile, 2) the temperature profile (T_z), 3) the surface temperature (T_s), and 4) the surface emissivity (ϵ_s). Perturbations to the relative humidity profile (-10%) and temperature profile (-2 K) were applied uniformly throughout the troposphere. Calculated brightness temperatures for each of the test cases are compared with results for the baseline state (described in the previous paragraph) in Table 1. As would be expected, perturbations to the surface parameters are reflected most strongly in the window channels, whereas perturbations in the meteorological profiles mainly affect the water vapor channels. Because the weighting function for the 183 ± 7 -GHz channel is substantially higher at the surface compared to the other water vapor channels (as seen in Fig. 3), it exhibits relatively stronger sensitivity to surface parameter perturbations and weaker sensitivity to meteorological profile perturbations.

Radiative transfer modeling results for the UM, GT, and GB cloud models are presented as brightness temperature contour plots in Figs. 4, 5, and 6. For each cloud model, LWP and IWP were independently varied between 0 and 500 g m^{-2} for a specific value of D_0 (either 200 or $400 \mu\text{m}$). All simulations were made for the nadir view. First-order radiative sensitivities to both LWP and IWP, that is, $\partial T_B / \partial \text{LWP}$ and $\partial T_B / \partial \text{IWP}$ are also presented in Tables 2 and 3. These derivatives individually represent the radiative sensitivity to one phase of the cloud in the absence of the other phase (i.e., $\partial T_B / \partial \text{LWP}$ is evaluated at zero IWP whereas $\partial T_B / \partial \text{IWP}$ is evaluated at zero LWP).

a. General observations

As seen in Figs. 4, 5, and 6, brightness temperatures for all of the water vapor channels tend to decrease monotonically both with increasing LWP and IWP. For these channels, increasing LWP tends to increasingly absorb upwelling radiance from below and reradiate at a relatively colder brightness temperature. In contrast, increasing IWP generally reduces the brightness temperature by reflecting upwelling radiation reaching the cloud bottom downward and reflecting the much weaker downwelling radiance at the cloud top upward.

TABLE 1. Comparison of clear-sky brightness temperature calculated for baseline atmospheric state (midlatitude winter) with clear-sky brightness temperatures calculated after applying perturbations to the tropospheric relative humidity, tropospheric temperature, surface temperature, and surface emissivity. Values in parentheses indicate difference between values for perturbed case and baseline state.

Perturbation	T_B (89)	T_B (150 GHz)	T_B (183 ± 7 GHz)	T_B (183 ± 3 GHz)	T_B (183 ± 1 GHz)
None	250.31	255.47	261.25	252.85	243.26
$\Delta \text{RH} = -10\%$	249.90 (-0.41)	254.48 (-0.99)	261.59 (0.34)	253.93 (1.08)	244.79 (1.53)
$\Delta T_z = -2.0$ K	250.11 (-0.20)	255.02 (-0.45)	259.45 (-1.80)	250.66 (-2.19)	241.09 (-2.17)
$\Delta T_s = -2.0$ K	248.76 (-1.55)	254.18 (-1.29)	260.93 (-0.32)	252.84 (-0.01)	243.26 (0.00)
$\Delta \epsilon_s = -0.05$	240.23 (-10.08)	248.46 (-7.01)	260.79 (-0.46)	252.84 (-0.01)	243.26 (0.00)

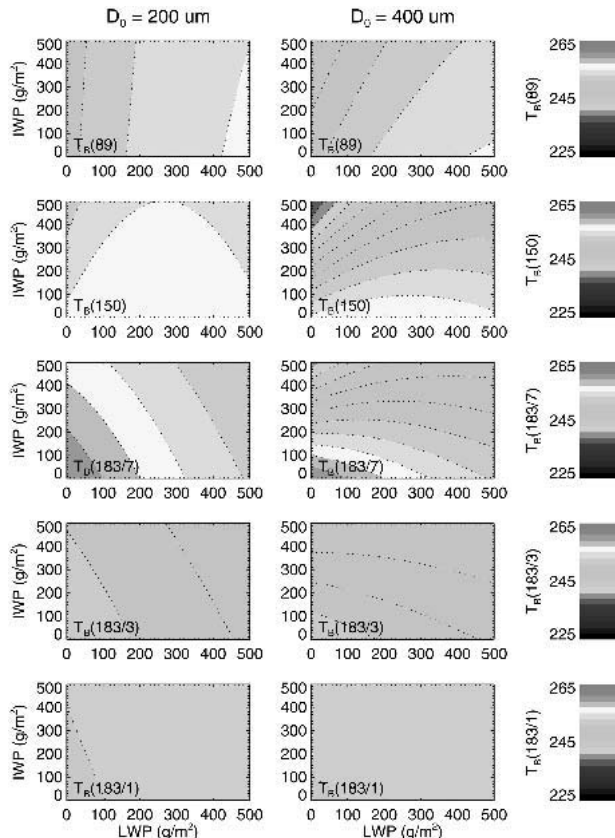


FIG. 4. AMSU-B brightness temperature contours for the UM mixed-phase cloud model with ice particle median diameters of 200 and 400 μm . Consecutive contours are separated in increments of 2 K.

For the window channels, however, increasing LWP tends to increase the brightness temperature. This trend is closely associated with the assumed surface emissivity (Greenwald et al. 1997; Jones and Vonder Haar 1990). Although the surface emissivity modulates both the thermal emission from the surface and the reflected downwelling radiation (through Kirchoff's law), its effect on the thermal emission term dominates for the window channels (as confirmed in Table 1). Thus, if the physical temperature of the surface is T_S , the effective radiative temperature of the surface is $\epsilon_S T_S$. In radiative terms, the surface may, therefore, appear much colder than the overlying atmosphere. Under these circumstances, increasing the absorption optical depth of the atmosphere (e.g., by increasing the LWP) will tend to "mask" the effectively colder surface, thereby increasing the brightness temperature observed at the top of the atmosphere. (This effect is even more dramatic over surfaces of open water, for which the emissivity is much smaller than it is for land.) In contrast, increasing IWP monotonically reduces the window channels' brightness temperatures by the same mechanism (scattering) described for the water vapor line channels.

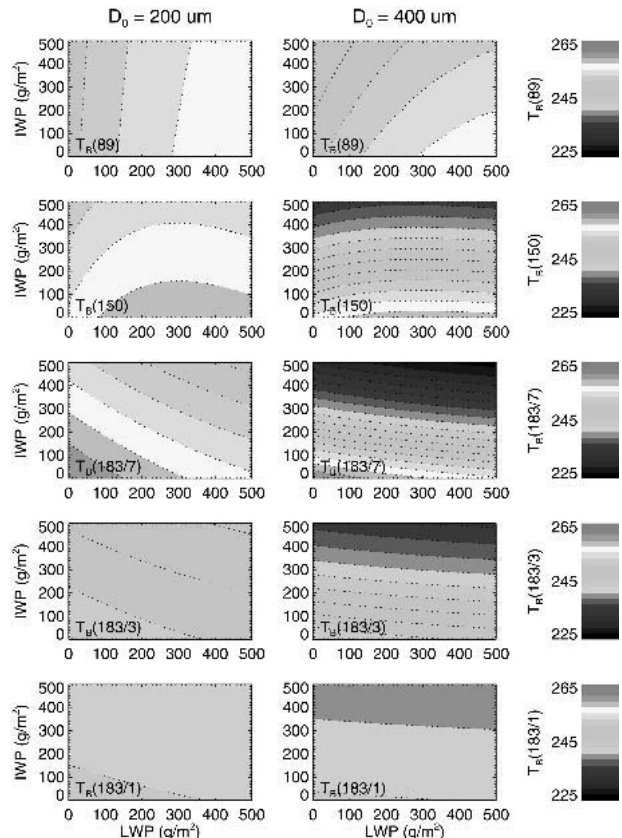


FIG. 5. As in Fig. 4 but for the GT mixed-phase cloud model.

b. Implications for retrieval algorithm development

The results of the simulations shown in Figs. 4, 5, and 6 and in Tables 2 and 3 have several implications for the development of millimeter-wave mixed-phase cloud classification and retrieval algorithms. First, comparison of the results for the GB and GT cloud models in Table 3 (where $IWP = 0$) reveals that vertical displacement of the 2-km-thick liquid cloud by 1 km has significant effects for both the window channels and the water vapor channels. For the window channels, sensitivity to LWP is greatest for the GT model, where the liquid is nearest the surface. For the water vapor channels, in contrast, the GB model exhibits the greatest LWP sensitivity. Thus, the window channels seem most sensitive to liquid cloud particles near the surface, whereas the 183 ± 7 -GHz channel is more sensitive to liquid in the midtroposphere. Generally, these results demonstrate that the validity of assumptions regarding the liquid phase vertical distribution will have a strong effect on the accuracy of millimeter-wave-based retrievals of LWP. Overall, the 183 ± 7 -GHz channel exhibits the highest LWP sensitivity $\partial T_B / \partial LWP$.

As indicated in Table 2 and in Figs. 5 and 6, the IWP sensitivity $\partial T_B / \partial IWP$ depends strongly on both the ice particle size and the vertical location of the ice layer. The strong increase in IWP sensitivity with increasing

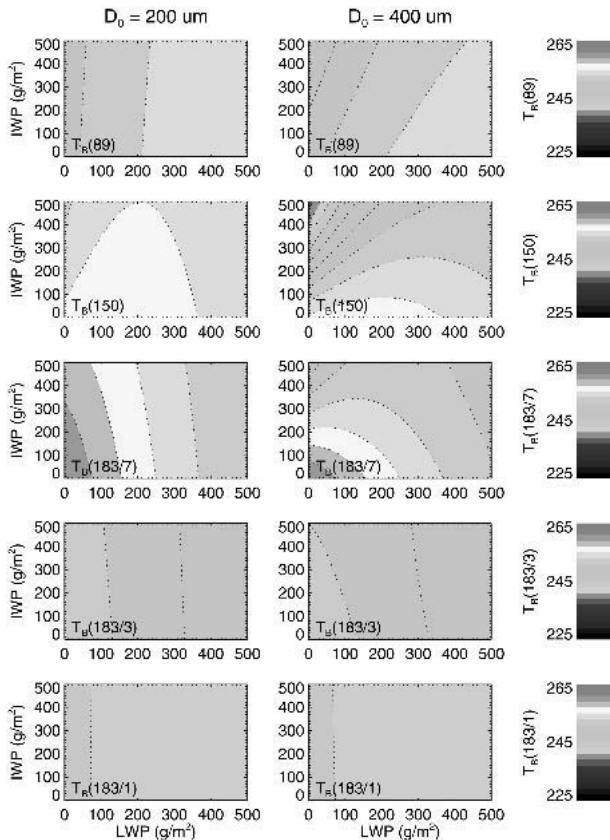


FIG. 6. As in Fig. 4 but for the GB mixed-phase cloud model.

particle size is a direct result of the nonlinear increase of extinction with particle size, as discussed in section 3b and shown in Fig. 2. Compared to the corresponding values of $\partial T_B/\partial \text{IWP}$ for $D_0 = 200 \mu\text{m}$, the values for $D_0 = 400 \mu\text{m}$ are approximately 8 times as large for the 89-GHz channel and 4 times as large for the water vapor channels. Thus, the water vapor channels exhibit weaker particle size dependence than the window channels. For the cloud models considered, the 183 ± 7 - and 150-GHz channels exhibit the greatest IWP sensitivity. Sensitivity to IWP increases with the altitude of the ice layer for all channels, because absorption and emission

TABLE 2. First-order radiative sensitivities [$\text{K} (\text{kg m}^{-2})^{-1}$] of AMSU-B channels to IWP ($\partial T_B/\partial \text{IWP}$) in three cloud models for two values of D_0 . Values are calculated for zero LWP.

Cloud model	D_0 (μm)	AMSU-B channel frequency (GHz)				
		89	150	183 ± 1	183 ± 3	183 ± 7
UM	200	-0.8	-6.9	-0.7	-4.0	-10.5
	400	-6.9	-38.3	-2.5	-15.3	-42.6
GB	200	-0.7	-6.2	-0.0	-1.1	-6.7
	400	-6.5	-35.3	-0.1	-4.2	-28.7
GT	200	-0.9	-7.7	-1.8	-8.1	-15.0
	400	-7.2	-42.6	-6.8	-35.1	-65.7

TABLE 3. First-order radiative sensitivities [$\text{K} (\text{kg m}^{-2})^{-1}$] of AMSU-B channels to LWP ($\partial T_B/\partial \text{LWP}$) in three cloud models. Values are calculated for zero IWP.

Cloud model	AMSU-B channel frequency (GHz)				
	89	150	183 ± 1	183 ± 3	183 ± 7
UM	18.3	12.2	-2.5	-10.9	-22.8
GB	15.5	7.4	-3.5	-14.5	-28.9
GT	21.2	17.7	-0.8	-6.2	-15.5

processes from both water vapor and liquid tend to mask the underlying atmosphere. As the ice layer is moved higher, there is less absorption to diminish the scattering effect of the ice layer. This effect is much more pronounced for the water vapor channels than for the window channels, as would be expected. For example, for the same D_0 , the IWP sensitivity $\partial T_B/\partial \text{IWP}$ for the 183 ± 7 -GHz channel more than doubles as the ice-layer base moves from 3 (in the GB model) to 5 (in the GT model) km.

In view of the large number of mixed-phase cloud parameters to which AMSU-B brightness temperatures are apparently sensitive, AMSU-B data alone are probably insufficient as the basis of a comprehensive mixed-phase cloud retrieval algorithm. The results above demonstrate that AMSU-B brightness temperatures are sensitive to cloud geometry (cloud boundaries for each phase), LWP, IWP, and ice particle size. Additional information, either from 1) complementary satellite or ground-based remote sensing instruments, 2) a priori data, or 3) modeling results would clearly be needed to retrieve basic mixed-phase cloud properties like LWP and IWP. Complementary remote sensing measurements might include satellite retrievals of cloud-top height and/or radar retrievals of cloud boundaries. A priori data might include statistics of in situ ice particle spectra measured under specific meteorological conditions.

5. Mixed-phase cloud case study

As discussed in section 2b, identifying and quantifying the effects of clouds in millimeter-wave satellite observations is much more challenging over land than over open water. Here, we present a case study to demonstrate that nonprecipitating mixed-phase clouds over land produce measurable effects on satellite millimeter-wave measurements. Comparisons of observed brightness temperatures with corresponding calculated clear-sky values reveal the effects of the clouds. These effects are quantified in terms of brightness temperature depression, that is,

$$\Delta T_B = T_B^{\text{calc}} - T_B^{\text{obs}}, \quad (10)$$

where T_B^{obs} and T_B^{calc} are the observed and corresponding calculated clear-sky brightness temperatures, respectively.

a. Ancillary data

The U.S. Department of Energy (DOE) operates an ongoing research program known as ARM. For studies of mixed-phase clouds, we exploited several datasets acquired at the ARM SGP Calibration and Radiation Test Bed (CART) site located in northern Oklahoma. The ARM data considered in this study were acquired from several ground-based instruments at the SGP Central Facility (36.605°N, 97.486°W) on 16 March 2002. Data from the ARM Millimeter-Wave Cloud Radar (MMCR; Moran et al. 1997) on this day were used to distinguish clear and cloudy periods, to locate cloud boundaries, and to identify periods of precipitation. MMCR radar reflectivity data are shown in Fig. 7. Retrievals from the 12-channel Microwave Radiometer Profiler (MWRP; Gueldner and Spaenkuch 2001; Liljegren et al. 2001b) provided local atmospheric temperature, water vapor, and liquid water content profiles at the times of the AMSU-B overpasses. As a source of meteorological profiles, MWRP retrievals were preferred over standard radiosonde data because of their much higher sampling frequency. As compared with radiosondes, the accuracy of MWRP temperature profiles is approximately 1°–2°C (rms), whereas MWRP water vapor profiles are generally at least accurate to 1–2 g m⁻³ (Liljegren et al. 2001b). For the period studied, MWRP retrievals were available approximately every 15 min, whereas soundings were only available approximately every 6 h. MWRP retrievals of LWP were supplemented by LWP retrievals from the two-channel Microwave Water Radiometer (MWR; Liljegren et al. 2001a), which has a longer operational history and has

been more extensively validated. Retrievals of LWP from both the MWR and MWRP instruments for 16 March 2002 are shown in Fig. 8.

Although the MMCR data shown in Fig. 7 exhibit periods of both clear and cloudy conditions, two distinct cloud layers are apparent. The higher cloud layer resides roughly between 6 and 10 km, whereas the lower cloud layer lies between 2 and 5 km. Analysis of these two cloud layers provides an important context for the ensuing analysis of the AMSU-B observations of this system. The location of the higher cloud layer suggests that it was most likely cirrus. This conjecture is supported by Geostationary Operational Environmental Satellite (GOES) retrievals (Minnis et al. 2001), which determined the cloud-top phase for the ARM SGP area during this day to be primarily ice. Additional evidence for the lack of liquid in the upper cloud layer is provided by the ground-based MWRP and MWR instruments. As shown in Fig. 8, retrievals of measurable amounts of liquid (e.g., LWP greater than 0.03 mm) for both instruments occur only between 1100 and 2000 UTC. These times correspond closely to the appearance and disappearance of the lower cloud layer, identifying that layer as the liquid-bearing layer. Moreover, inspection of the MWRP liquid water content vertical profiles between 1100 and 2000 UTC indicates that the cloud liquid is heavily concentrated between the surface and about 4 km. The consistent picture emerging from all of these datasets is a two-layer cloud system consisting of either a liquid or mixed-phase cloud in the midtroposphere below a separated layer of thick cirrus. Last, the high peak radar reflectivity values observed in the lower cloud layer (often greater than 10 dBZ)

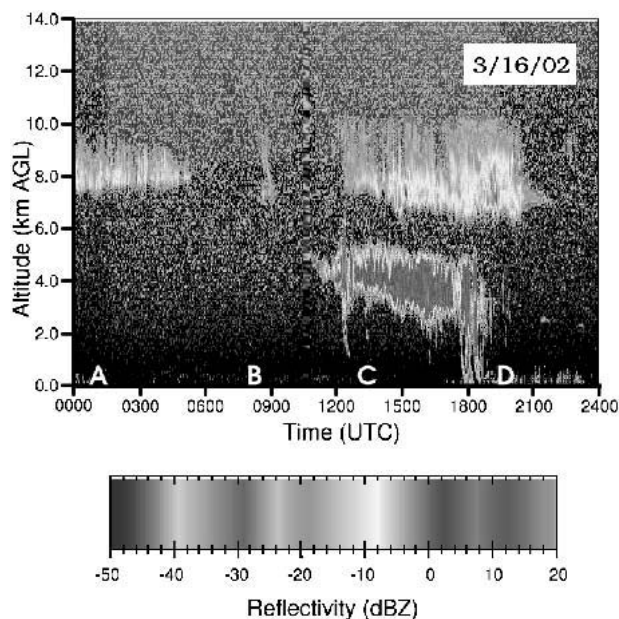


FIG. 7. Radar reflectivity recorded by the MMCR at the ARM SGP field site on 16 Mar 2002.

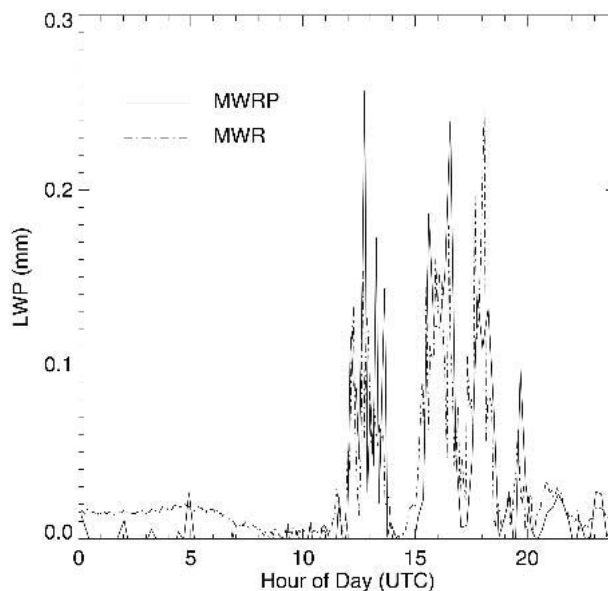


FIG. 8. Retrievals of liquid water path for both the 2-channel MWR and 12-channel MWRP instruments at the ARM SGP field site on 16 Mar 2002.

strongly suggest the presence of ice particles (Vivekanandan et al. 1999). We, therefore, conclude that the lower cloud was mixed in phase. The radar data further indicate that, with the possible exception of a brief period at approximately 1800, this cloud system was not precipitating. No measurable precipitation was observed at the SGP Central Facility surface station on this day.

b. AMSU-B data

All of the AMSU-B observations from both the NOAA-K and -L satellites falling within a 1° latitude \times 1° longitude box centered on the SGP Central Facility on 16 March 2002, were collected. A total of 89 AMSU-B observations derived from four satellite overpasses were found and analyzed. Satellite overpasses occurred at approximately 0105, 0810, 1325, and 1935 UTC, which are labeled hereinafter (and in Fig. 7) as “A,” “B,” “C,” and “D,” respectively. According to arguments presented in the previous paragraph, overpass A corresponds to a period of cirrus cover. Overpass B occurred during a period of clear sky, just before the brief appearance of cirrus. Overpass C corresponds to a period during which both cloud layers were well developed. Overpass D occurred after the disappearance of the lower cloud, but the cirrus layer was still clearly evident. Because the lower cloud layer was absent for overpasses A, B, and D, those overpasses are collectively termed the “cirrus scenes.” Overpass C is the sole satellite overpass during which the mixed-phase cloud was observed.

For each actual AMSU-B observation, corresponding clear-sky brightness temperatures were calculated using the radiative transfer model described in section 3. Actual satellite zenith angles for each observation along with temperature and water vapor profiles obtained from the MWRP were fed to the model to estimate the clear-sky brightness temperatures. A surface emissivity of 0.95 was assumed for all model calculations. This value was selected because 1) it is well within the range of reported microwave surface emissivity values over land (Felde and Pickle 1995) and 2) it produced reasonable agreement between the observed and calculated brightness temperatures for the three cirrus scenes at both 89 and 150 GHz. Studies based on modeling results (Muller et al. 1994) and airborne observations (Wang et al. 1998) indicate that cirrus-induced brightness temperature depressions at 89 GHz are typically less than a few kelvin. For the purpose of estimating surface emissivity, we neglected the radiative effects of cirrus entirely. For each observation and AMSU-B channel, ΔT_B provides a quantitative measure of the net radiative effect of the clouds within the AMSU-B field of view.

Comparisons of observed AMSU-B brightness temperatures with corresponding calculated clear-sky values are presented as scatterplots in Fig. 9. Unique plotting symbols (defined in the figure caption) distinguish

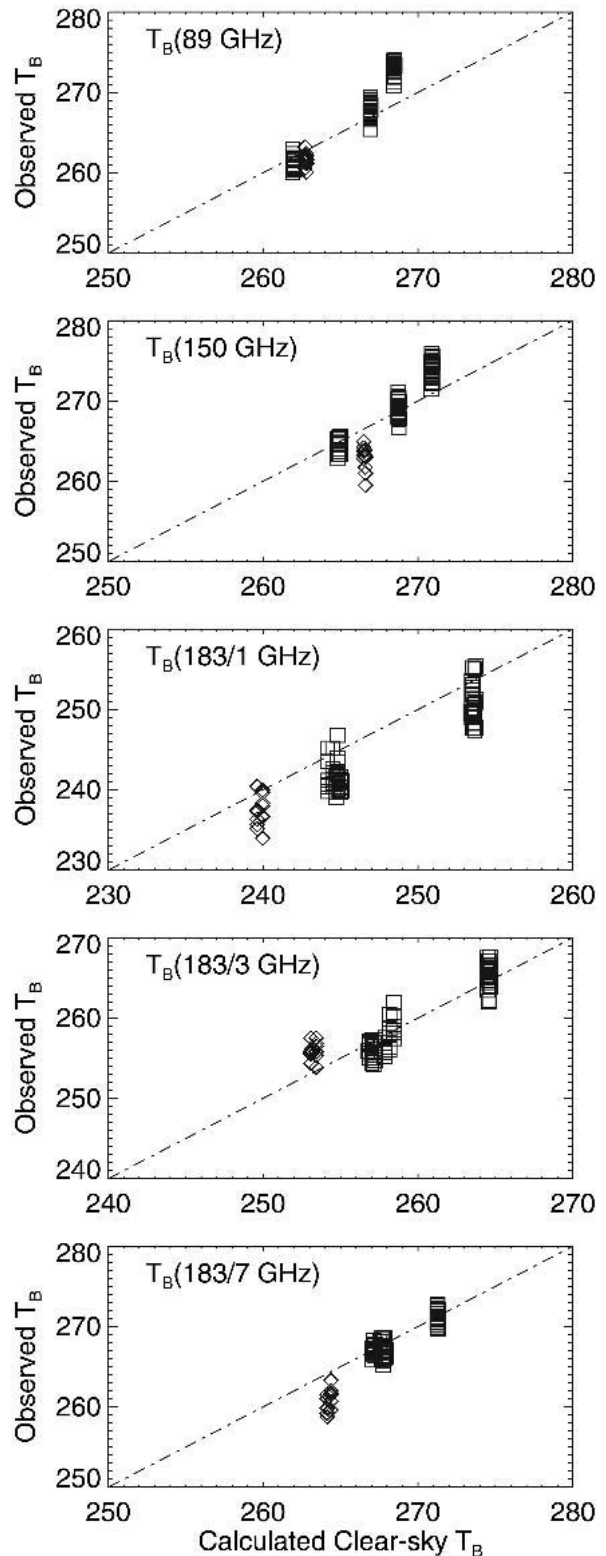


FIG. 9. Comparison of observed and model-calculated AMSU-B brightness temperatures at the ARM SGP site for 16 Mar 2002. Data for mixed-phase cloud overpass at 1325 UTC are plotted with the \diamond symbol. Results for cirrus-scene overpasses are plotted with the \square symbol.

the AMSU-B observations made during overpass C from the other three overpasses. The ΔT_B statistics (both means and standard deviations) were calculated separately for overpass C and the other three overpasses and are listed in Table 4.

c. Analysis

For the 89- and 150-GHz channels, absolute deviations between the observed and calculated clear-sky brightness temperatures in the three cirrus scenes are typically only a few kelvin. (For these channels, the assumed surface emissivity value directly affects the systematic bias between the observed brightness temperatures and corresponding calculated clear-sky brightness temperatures, but has no effect on the bias of ΔT_B values for overpass C relative to the three cirrus scenes.) At 89 GHz, ΔT_B statistics for overpass C generally agree with values for the cirrus scenes. However, for the 150-GHz channel, an overall ΔT_B bias of 4.6 K is observed between overpass C and the other three overpasses (as seen in Table 4), with a maximum ΔT_B value of about 7 K. Qualitatively, the stronger effect of the mixed-phase cloud on the 150-GHz channel relative to the 89-GHz channel agrees with modeling results presented in section 4.

Because of the strong frequency dependence of the single scattering properties of ice particles (as shown in Fig. 2), cirrus-induced brightness temperature depressions are potentially much greater for the water vapor channels than for the window channels (Muller et al. 1994; Wang et al. 1998). For these channels more than for the window channels, absorption and emission by water vapor in and above any cirrus cloud would reduce the brightness temperature depression caused by the cloud. Thus, cirrus-induced brightness temperature depressions for the water vapor channels depend on the position of the ice layer relative to each of the water vapor channels' weighting functions. For example, if the cirrus layer resides well above the peaks of the weighting functions for all three water vapor channels, cirrus-induced brightness temperature depressions will be approximately the same for all three channels. In conditions where the cirrus layer is not well above the water vapor channel weighting functions, the masking effect of water vapor (which tends to reduce brightness temperature depression) in and above the cirrus layer will be strongest for the 183 ± 1 -GHz channel and weakest for the 183 ± 7 -GHz channel. Thus, the $183 \pm$

7-GHz channel should generally be the most cirrus-sensitive AMSU-B channel. The lack of any appreciable brightness temperature depressions (i.e., larger than a few kelvin) at 183 ± 7 GHz for the three cirrus scenes indicates that the cirrus layer had negligible effect on the AMSU-B data analyzed in this paper.

Retrievals of temperature and water vapor profiles from the ground-based MWRP were used in model calculations instead of radiosonde data because of the much greater sampling frequency. (Any benefits that might be gained from using radiosonde data for this purpose would be greatly outweighed by large errors encountered because of the lack of synchronicity between the radiosonde measurements and the AMSU-B observations. Moreover, the much higher vertical resolution offered by the radiosonde measurements is relatively unimportant for simulating millimeter-wave brightness temperatures, which respond to water vapor averaged over thick layers.) MWRP water vapor profiles exhibit relative errors that increase with altitude (Liljegren 2004). This effect, combined with the water vapor channels' weighting functions (as shown in Fig. 3), implies that water vapor profile uncertainties should typically produce the largest errors in calculated brightness temperatures for the 183 ± 1 -GHz channel and the smallest errors in calculations for the 183 ± 7 -GHz channel. This expectation is confirmed in the three cirrus scenes (plotted in Fig. 9 with the \square symbol). This characteristic of the ancillary data implies that smaller cloud-induced ΔT_B values should be resolvable for the 183 ± 7 -GHz channel than for the 183 ± 1 - and 183 ± 3 -GHz channels.

Comparing the water vapor channels only, the results presented graphically in Fig. 9 and statistically in Table 4 show that the mixed-phase cloud present during overpass C produces the most obvious effect at 183 ± 7 GHz. For this channel, the overall bias between ΔT_B values for overpass C and the three cirrus-scene overpasses of 3.2 K is nearly 4 times as large as the standard deviation of the cirrus-scene ΔT_B values. The maximum ΔT_B value of approximately 6 K is nearly 2 times as large as the largest value for the three cirrus scenes. In contrast, for both the 183 ± 1 - and 183 ± 3 -GHz channels, ΔT_B values for overpass C fall well within the range of values for the other three overpasses.

The results of this case study qualitatively agree with the modeling results presented in section 4 in that 1) brightness temperature sensitivities to both LWP and

TABLE 4. Comparison of AMSU-B ΔT_B statistics at ARM SGP site on 16 Mar 2002 for 1) mixed-phase cloud observations (overpass C) and 2) three cirrus scenes (overpasses A, B, and D).

	AMSU-B channel frequency (GHz)				
	89	150	183 ± 1	183 ± 3	183 ± 7
ΔT_B^C	-1.10 ± 0.78	-3.57 ± 1.44	-2.43 ± 1.82	2.52 ± 1.09	-3.52 ± 1.27
ΔT_B^{ABD}	1.71 ± 2.29	1.00 ± 1.84	-3.09 ± 1.97	-0.15 ± 1.53	-0.32 ± 0.87

IWP are stronger at 150 than at 89 GHz, and 2) among the three water vapor channels, the largest brightness temperature depressions occur for the 183 ± 7 -GHz channel. These results also demonstrate empirically that real mixed-phase clouds over land can produce measurable effects on AMSU-B measurements.

6. Conclusions

A wide range of geophysical parameters affect observations from satellite-based millimeter-wave radiometers (such as AMSU-B), including surface temperature and emissivity, atmospheric temperature and water vapor profiles, clouds, and precipitation. Thus, the usefulness of each of the AMSU-B channels for studying mixed-phase clouds depends not only on the sensitivity of brightness temperatures to mixed-phase cloud properties, but also the availability of precise ancillary data. The 89- and 150-GHz channels are rather insensitive to atmospheric temperature and water vapor, but highly sensitive to surface temperature and emissivity. Conversely, the three AMSU-B water vapor channels at $183 \pm 1, 3,$ and 7 GHz, are relatively insensitive to the surface but are much more sensitive to the atmospheric temperature and water vapor profiles. In terms of single scattering properties only, the water vapor channels are more sensitive to both liquid and ice particles than are the 89- and 150-GHz channels.

A case study was presented to demonstrate the potential of AMSU-B observations for studying mixed-phase clouds over land. A key aspect of this study was the availability of temperature and water vapor profiles (from a ground-based remote sensing instrument) matched in time and space with the AMSU-B observations. Comparisons of observed and calculated clear-sky AMSU-B brightness temperatures at the ARM SGP site demonstrate that a mixed-phase cloud produced measurable brightness temperature depressions at the 150- and 183 ± 7 -GHz channels.

Retrieval algorithms designed to exploit millimeter-wave observations for cloud studies have so far only considered single-phase systems, that is, pure liquid clouds or pure ice clouds. Mixed-phase cloud simulation results presented here indicate that both phases of water can produce significant effects on the observed brightness temperatures for all AMSU-B channels. Therefore, retrieval algorithms developed to retrieve properties (such as IWP) of one particular phase should not be applied to mixed-phase clouds.

The development of mixed-phase cloud classification or retrieval schemes based on AMSU-B data might follow one of three approaches. In the first approach, necessary ancillary data would be provided by other satellite-based remote sensing instruments. This is the approach taken by Rosenkranz (2001), who developed a retrieval algorithm for liquid-only clouds based on AMSU-A and AMSU-B observations. This approach

might also benefit from thermal infrared observations, which are used routinely for determining cloud-top height. The second approach would involve the use of water vapor and temperature profiles generated by numerical weather prediction models. Further work is needed to assess the classification or retrieval errors that would result from the use of these models. Last, the third alternative would be to combine AMSU-B data with observations from ground-based remote sensing instruments. Although such an approach would only yield retrieval results over limited regions, ground-based instruments (such as the MWRP) often provide measurements that are not feasible from space-based platforms.

Acknowledgments. Portions of this research were sponsored by the National Science Foundation through an interagency agreement in response to requirements and funding by the Federal Aviation Administration's Aviation Weather Research Program. The views expressed are those of the authors and do not necessarily represent the official policy or position of the U.S. Government. Data used in this study were obtained from the Atmospheric Radiation Measurement (ARM) Program sponsored by the U.S. Department of Energy, Office of Science, Office of Biological and Environmental Research, Environmental Sciences Division.

REFERENCES

- Baum, B. A., P. F. Soulen, K. I. Strabala, M. D. King, S. A. Ackerman, W. P. Menzel, and P. Yang, 2000: Remote sensing of cloud properties using MODIS airborne simulator imagery during SUCCESS. II. Cloud thermodynamic phase. *J. Geophys. Res.*, **105**, 11 781–11 792.
- Burns, B. A., X. Wu, and G. R. Diak, 1997: Effects of precipitation and cloud ice on brightness temperatures in AMSU moisture channels. *IEEE Trans. Geosci. Remote Sens.*, **35**, 1429–1437.
- Cober, S. G., G. A. Isaac, A. V. Korolev, and J. W. Strapp, 2001: Assessing cloud-phase conditions. *J. Appl. Meteor.*, **40**, 1967–1983.
- Deeter, M. N., and K. F. Evans, 1998: A hybrid Eddington-single scattering radiative transfer model for computing radiances from thermally emitting atmospheres. *J. Quant. Spectrosc. Radiat. Transfer*, **60**, 635–648.
- , and —, 2000: A novel ice-cloud retrieval algorithm based on the Millimeter-wave Imaging Radiometer (MIR) 150- and 220-GHz channels. *J. Appl. Meteor.*, **39**, 623–633.
- Ellingson, R. G., J. Ellis, and S. Fels, 1991: The intercomparison of radiation codes used in climate models: Long wave results. *J. Geophys. Res.*, **96**, 8929–8953.
- Evans, K. F., and J. Vivekanandan, 1990: Multiparameter radar and microwave radiative transfer modeling of nonspherical atmospheric ice particles. *IEEE Trans. Geosci. Remote Sens.*, **38**, 423–437.
- , and G. L. Stephens, 1995: Microwave radiative transfer through clouds composed of realistically shaped ice crystals. Part I: Single scattering properties. *J. Atmos. Sci.*, **52**, 2041–2057.
- , S. J. Walter, A. J. Heymsfield, and M. N. Deeter, 1998: Modeling of submillimeter passive remote sensing of cirrus clouds. *J. Appl. Meteor.*, **37**, 184–205.
- Felde, G. W., and J. D. Pickle, 1995: Retrieval of 91 and 150 GHz

- earth surface emissivities. *J. Geophys. Res.*, **100**, 20 855–20 866.
- Fleishauer, R. P., V. E. Larson, and T. H. Vonder Haar, 2002: Observed microphysical structure of midlevel, mixed-phase clouds. *J. Atmos. Sci.*, **59**, 1779–1804.
- Gasiewski, A. J., 1993: Microwave radiative transfer in hydrometeors. *Atmospheric Remote Sensing by Microwave Radiometry*, M. A. Janssen, Ed., John Wiley and Sons, 572 pp.
- Goody, R. L., and Y. L. Yung, 1995: *Atmospheric Radiation: Theoretical Basis*. 2d ed. Oxford University Press, 519 pp.
- Greenwald, T. J., C. L. Combs, A. S. Jones, D. L. Randel, and T. H. Vonder Haar, 1997: Further developments in estimating cloud liquid water over land using microwave and infrared satellite measurements. *J. Appl. Meteor.*, **36**, 389–405.
- , S. A. Christopher, J. Chou, and J. C. Liljegren, 1999: Intercomparison of cloud liquid water path derived from the GOES 9 imager and ground based microwave radiometers for continental stratocumulus. *J. Geophys. Res.*, **104**, 9251–9260.
- Gueldner, J., and D. Spaenkuch, 2001: Remote sensing of the thermodynamic state of the atmospheric boundary layer by microwave radiometry. *J. Atmos. Oceanic Technol.*, **18**, 925–933.
- Isaacs, R. G., and G. Deblonde, 1987: Millimeter wave moisture sounding: The effect of clouds. *Radio Sci.*, **22**, 367–377.
- Jet Propulsion Laboratory, 2000: AIRS project algorithm theoretical basis document, level 1b, part 3: Microwave instruments, version 2.1. California Institute of Technology Publication JPL D-17005, 59 pp.
- Jones, A. S., and T. H. Vonder Haar, 1990: Passive microwave remote sensing of cloud liquid water over land regions. *J. Geophys. Res.*, **95**, 16 673–16 683.
- Liljegren, J. C., 2004: Improved retrievals of temperature and water vapor profiles with a twelve-channel radiometer. *Preprints, Eighth Symp. on Integrated Observing and Assimilation Systems for Atmosphere, Oceans, and Land Surface (IOAS-AOLS)*, Seattle, WA, Amer. Meteor. Soc., CD-ROM, 4.7.
- , E. E. Clothiaux, G. G. Mace, S. Kato, and X. Dong, 2001a: A new retrieval for cloud liquid water path using a ground-based microwave radiometer and measurements of cloud temperature. *J. Geophys. Res.*, **106**, 14 485–14 500.
- , B. M. Lesht, S. Kato, and E. E. Clothiaux, 2001b: Evaluation of profiles of temperature, water vapor, and cloud liquid water from a new microwave radiometer. *Proc. 11th ARM Science Team Meeting*, Atlanta, GA, U.S. Department of Energy.
- Liou, K. N., 1992: *Radiation and Cloud Processes in the Atmosphere*. Oxford University Press, 487 pp.
- Liu, G., and J. A. Curry, 2000: Determination of ice water path and mass median particle size using multichannel microwave measurements. *J. Appl. Meteor.*, **39**, 1318–1329.
- Minnis, P., W. L. Smith Jr., and D. F. Young, 2001: Cloud macro- and microphysical properties derived from GOES over the ARM SGP domain. *Proc. 11th ARM Science Team Meeting*, Atlanta, GA, U.S. Department of Energy.
- Moran, K. P., B. E. Martner, D. C. Welsh, D. A. Merritt, M. J. Post, and T. Uttal, 1997: ARM's cloud-profiling radar. *Preprints, 28th Conf. on Radar Meteorology*, Austin, TX, Amer. Meteor. Soc., 296–297.
- Muller, B. M., H. E. Fuelberg, and X. Xiang, 1994: Simulations of the effects of water vapor, cloud liquid water, and ice on AMSU moisture channel brightness temperatures. *J. Appl. Meteor.*, **33**, 1133–1154.
- Politovich, M. K., 1989: Aircraft icing caused by large supercooled droplets. *J. Appl. Meteor.*, **28**, 856–868.
- Ray, P. S., 1972: Broadband complex refractive indices of ice and water. *Appl. Opt.*, **11**, 1836–1844.
- Riley, R. K., 1998: Mixed-phase icing conditions: A review. U.S. Dept. of Transportation Rep. DOT/FAA/AR-98/76, 45 pp.
- Rosenkranz, P. W., 2001: Retrieval of temperature and moisture profiles from AMSU-A and AMSU-B measurements. *IEEE Trans. Geosci. Remote Sens.*, **39**, 2429–2435.
- Vivekanandan, J., L. Li, L. Tsang, and C. Chan, 1997: Microwave radiometric technique to retrieve vapor, liquid and ice: Part II—Joint studies of radiometer and radar in winter clouds. *IEEE Trans. Geosci. Remote Sens.*, **35**, 237–247.
- , B. E. Martner, M. K. Politovich, and G. Zhang, 1999: Retrieval of atmospheric liquid and ice characteristics using dual-wavelength radar observations. *IEEE Trans. Geosci. Remote Sens.*, **37**, 2325–2333.
- Wang, J. R., P. Racette, J. D. Spinhirne, K. F. Evans, and W. D. Hart, 1998: Observations of cirrus clouds with airborne MIR, CLS, and MAS during SUCCESS. *Geophys. Res. Lett.*, **25**, 1145–1148.
- Westwater, E. R., 1993: Ground-based microwave remote sensing of meteorological variables. *Atmospheric Remote Sensing by Microwave Radiometry*, M. A. Janssen, Ed., John Wiley and Sons, 572 pp.
- Zhang, G., and J. Vivekanandan, 1999: Microwave radiation from mixed phase cloud and parameter retrievals. *Proc. Int. Geoscience and Remote Sensing Symp.*, Hamburg, Germany, IEEE, 2182–2184.
- Zhao, L., and F. Weng, 2002: Retrieval of ice cloud parameters using the Advanced Microwave Sounding Unit. *J. Appl. Meteor.*, **41**, 384–394.